Physica Scripta

PAPER • **OPEN ACCESS**

A first-principles study of the electronic, mechanical, vibrational, and optical properties of the zirconium carbide under high pressure

To cite this article: H Muñoz *et al* 2023 *Phys. Scr.* **98** 025817

IOP Publishing Phys. Scr. 98 (2023) 025817 https://doi.org/10.1088/1402-4896/acb326

Physica Scripta

RECEIVED
21 September 2022

REVISED
6 December 2022

ACCEPTED FOR PUBLICATION
15 January 2023

PUBLISHED
24 January 2023

PAPER

A first-principles study of the electronic, mechanical, vibrational, and optical properties of the zirconium carbide under high pressure

H Muñoz[1], J E Antonio[1], J M Cervantes[2], M Romero[3], J L Rosas-Huerta[4], E P Arévalo-López[3], E Carvajal[1,*] and R Escamilla[2,*]

[1] Escuela Superior de Ingeniería Mecánica y Eléctrica-Culhuacán, Instituto Politécnico Nacional, Av. Santa Ana 1000, Ciudad de México, 04440, Mexico
[2] Instituto de Investigaciones en Materiales, Universidad Nacional Autónoma de México. Apartado Postal 70-360, Ciudad de México, 04510, Mexico
[3] Facultad de Ciencias, Universidad Nacional Autónoma de México, Apartado Postal 70-399, México Ciudad de México, 04510, Mexico
[4] Unité de Catalyse et Chimie du Solide (UCCS) - UMR CNRS 8181, Université de Lille - Centrale Lille, ENSCL, Lille, F-59000, France
[*] Authors to whom any correspondence should be addressed.

E-mail: ecarvajalq@ipn.mx and rauleg@unam.mx

Keywords: DFT, high pressure, phase transition, zirconium carbide, phonons, optical

Abstract

Zirconium carbide is a compound widely used in cutting tools, nuclear reactors, field emitter arrays and solar energy receivers; additionally, combined with other materials, it can be used in rocket technology and the aerospace industry. For this work was studied the effect of the high hydrostatic pressure on the electronic, mechanical, vibrational, and optical properties of the ZrC, from first principles calculations based on the Density Functional Theory. The calculated enthalpy and cohesive energy data show a B1 (NaCl) to B2 (CsCl) phase transition at 297 GPa. For the B1 phase, results for the calculated equilibrium lattice parameters, bands structure, electron and phonon densities of states, elastic moduli constants, entropy, enthalpy, Gibbs free energy, heat capacity, reflectivity, loss function, conductivity, and dielectric function are consistent with the available experimental and theoretical data. Our results for phonons show that the B1 phase is dynamically stable; in contrast, the B2 phase is not stable. Furthermore, when pressure is applied, the calculated density of electronic states shows that the C $2p$-orbitals around the Fermi energy contribute significantly to the conduction band, turning the compound into a ductile the material, with a mixture of metallic and ionic-covalent bonds. On the other hand, the study of the mechanical properties of the B1 phase shows a highest mechanical resistance and maximum thermal absorption, above 356 K and 638 K, respectively; but these switch to higher temperatures as pressure is applied. Finally, the B1 phase of the ZrC is a good coating material and a photon detector at low frequencies in the UV region, but also at the visible and infrared regions; although, increasing the pressure, the values of the optical properties increase. The increase of the parameters' values of the studied properties, as the pressure increases, indicates that the ZrC could be more efficient in a wider range of applications.

1. Introduction

The transition metal carbides (TMC) have attracted attention because these are materials with peculiar thermal, electronic, and mechanical properties [1]; among these properties, the high melting point (around 3670 K [2]) is too notorious and allows to tag the TMC as refractory carbides [3]. Another properties linked to the TMC are the extreme hardness, the superconductivity, the magnetic susceptibility, and the electrical and chemical resistance; all these properties make those compounds very attractive for many technological applications, as: high-speed steel cutting tools, information storage, spintronic devices and protective coatings for optical and mechanical components. Also, those carbides are used in the petroleum and aerospace industries [3–7]. The more stable phase crystallization, for most of the TMC, is the rock salt type (B1), which exhibits a contribution mixture from covalent, ionic, and metallic bonds. The covalent character interaction among the transition metal (TM) 3*d*- and the carbon (C) 2*p*-orbitals is the origin of the unusual hardness associated with the TMC. On the other hand, a charge transfer from the TM to the C atoms causes ionic bonds, while the TM states near the Fermi level generate metallic bonds [8, 9].

Theoretical studies on the ZrC have predicted a possible structural phase transition (P_T) from the B1 to the B2 (CsCl), around 300 GPa; however, to our knowledge, there are no experimental reports that advance pressures higher than 100 GPa [3–5, 10–12]. Although there are some theoretical studies on the electronic and vibrational properties at the B1 to the B2 phase transition under pressure, there is no one systematic study on the electronic, mechanical, vibrational, and optical properties under pressure. Therefore, for this work, it was proposed to study these properties at the B1 to B2 phase transition under pressure.

The manuscript is organized as follows: the calculation scheme, and the theory to obtain the properties mentioned earlier, are described in section 2; the results and discussion of the most stable magnetic behavior and the structural, electronic, mechanical, vibrational, thermodynamical, and optical properties of the studied compounds, are provided in section 3. Finally, the conclusions from the obtained results are discussed in section 4.

2. Methodology

2.1. Calculations details

Calculations for this work were performed within the DFT scheme [13], using the Cambridge Sequential Total Energy Package (CASTEP) code [14, 15]. The electronic exchange-correlation was treated using the Perdew-Wang (PW91) functional [16] parameterization by the Generalized Gradient Approximation (GGA). The core electrons were represented using Vanderbilt-type ultrasoft pseudo-potentials [17] and the system's minimum energy configuration was obtained using a plane waves basis. The Broyden-Fletcher-Goldfarb-Shanno's (BFGS) algorithm was used for the geometry optimization [18]. The convergence tolerances were fixed as follows: cut-off energy was 500 eV, the Brillouin zone (BZ) was sampled using $9 \times 9 \times 9$ k-grids on the Monkhorst-Pack scheme [19], a maximum force on the atoms of 0.01 eV Å^{-1}, ionic displacement of 5×10^{-3} Å, and the highest strain amplitude of 0.02 GPa. The different magnetic configurations (MC) were studied according to the following criteria: the formal spin was not considered for the paramagnetic (PM) configuration; the B1 phase is a ferromagnetic (FM) order; and the A, C, and G type antiferromagnetic (AFM) behaviors were modeled as in [20]; whereas the B2 FM phase and G-type AFM were modeled as described in [21]. Calculation of the second-order inner elastic constants was made using the method of homogeneous deformations. The phonon and optical properties were calculated using cut-off energy of 680 eV and a BZ sampled by $4 \times 4 \times 4$ k-grids at the Monkhorst-Pack scheme. The phonon dispersion curves were implemented under the density functional perturbation theory (DFPT), using the finite displacement method with norm-conserving pseudo-potentials with a cut-off radius of 4 Å. Calculation of the optical properties was made with a plasma frequency of 10 eV for the polarization vector [1 0 0].

2.2. Theory

To analyze the structural properties of the ZrC, under pressure, the volume and lattice parameters were normalized, using as reference those for the systems at zero GPa, as it was described in [22, 23]. The Gibbs' free energy relationship was used to determine the P_T value associated with the ZrC's structural phase change; nevertheless, when T = 0 K, the Gibbs' free energy is equal to the enthalpy (*H*):

$$H = U + PV \tag{1}$$

where *U* is the internal energy, *P* is the pressure and *V* is the volume. The cohesive energy (E_{coh}) [24] per atom was chosen as the thermodynamic stability criterion, and this is defined by:

$$E_{coh} = ((nE_{Zr} + mE_C - E_{total}))/((n + m)) \tag{2}$$

being E_{Zr} and E_C the total energies for isolated Zr and C atoms; *n* and *m* the number of Zr and C atoms, respectively, in the system's cells; and E_{total} is the ground-state total energy for the ZrC.

The elastic constants (C_{ij}) were used to define the materials' mechanical resistance, as well as the stability of the elastic materials' phase. Therefore, three independent second-order elastic constants (SOEC) were determined: C_{11}, C_{12}, and C_{44}; and their SOEC'values must satisfy the following mechanical stability criteria [5]:

$$(C_{11} - C_{12}) > 0 \tag{3}$$

$$(C_{11} + 2C_{12}) > 0 \tag{4}$$

$$C_{11} > 0 \tag{5}$$

$$C_{44} > 0 \tag{6}$$

On the other hand, the bulk (B_0) and shear (G) Hill's moduli provide information on the hardness of the material, concerning different types of deformation. In contrast, Young's modulus (Y) is a measure of the material's elastic behavior, subjected to a tensile or compressive force. The formulas to obtain these values can be found in many references [9, 25]. The Pugh's and Poisson's ratios indicate the ductility and brittleness of a material [26]: Pugh's ratio values greater than 0.5 are linked to brittle materials, and lower values are linked to ductile materials [27–29]; the relevant values for the Poisson's ratio (ν) are those $\geqslant 0.33$ for metals, while those from 0.16 to 0.30 are related to ionic-covalent compounds [27–29]. Vickers hardness (H_V) is a measure used to determine the hardness of a material [30], and the K, ν, and H_V values can be obtained using:

$$K = G/B_0 \tag{7}$$

$$\nu = ((3B_0 - Y))/(6B_0) \tag{8}$$

$$H_V = 0.92K^{1.137}G^{0.708} \tag{9}$$

Thermal energy or external forces produce vibrations at the material's lattice. These mechanical waves called phonons are responsible for transporting heat and sound through the crystal [31]. The frequency (ω) dependence on the wave vector is known as the phonon dispersion (PD), and the phonon dispersion relations were achieved within the linear response theory to calculate the response to periodic perturbations [32, 33]. The PD was obtained by finite displacements of atomic planes, using a combination of supercells, maximized by a cut-off radius of the force constants [34]. The phonon dispersion was calculated assuming that the mean equilibrium position of each ion in a BZ site, and the amplitude of the atomic displacements, are small compared to the interatomic distances. The phonons' properties are described using the harmonic approximation (equation (10)) based on the dynamical matrix related to the interatomic force constants [35]:

$$D_{\alpha i,\beta j}(q) = (1/(M_i M_j)^{1/2})\sum_R C_{\alpha i,\beta j}(R)\exp(-iq\cdot R) \tag{10}$$

The dynamical matrix ($D_{\alpha i,\beta j}$) depends on the mass of the ith and jth atoms ($M_i\,M_j$), the force constants ($C_{\alpha i,\beta j}$) and the summation over the lattice vectors within the cut-off radius (R).

The finite displacement method allows to calculate the constant force matrix using the difference equation described in [35]. Usually, the phonons are described calculating their values at points in the first BZ [36]. There will be 3 N phonons per k-point. The lowest three modes represent the acoustic branch; these modes correspond to the translation of the crystal lattice and tend to a value of zero at the Γ point. This behavior is characteristic of sound waves. The remaining vibrational modes (3 N−3) are optical modes because they can interact with electromagnetic radiation in ionic crystals. Unlike the acoustic modes, the frequencies of optical modes are finite at the point $q = 0$. The crystal structure is dynamically unstable when the PD curves have imaginary (negative) frequencies or soft phonon modes [37].

The minimized Helmholtz free energy, concerning all its geometric freedom degrees {ai} without external pressure, can be found for any temperature (T) as $F(\{ai\},T) = U - TS$. For the perfectly harmonic crystal, its U was replaced by the sum of the ground-state total energy (E_{tot}), and the second term was replaced by the vibrational free energy (E_{vib}) [38]:

$$F(T) = E_{tot} + E_{vib} \tag{11}$$

If anharmonic effects are not considered, the phonon frequencies do not depend on the lattice parameters; consequently, the free energy dependence on the structure is enclosed only in E_{tot}. On the other hand, the zero-point vibrational energy (E_{zp}), the phonon density of states ($F(\omega)$), the Boltzmann constant (k_B), and the Planck constant (ħ) are part of the E_{vib} (T):

$$F(T) = E_{tot} + E_{zp} + k_B T\int F(\omega)\ln[1 - \exp(-\hbar\omega/k_B T)]d\omega \tag{12}$$

where E_{zp} can be evaluated as

$$E_{zp} = (1/2)\int F(\omega)\hbar\omega d\omega \tag{13}$$

The contribution from vibrational entropy (S) can be calculated using the following formula [35]:

$$S(T) = k_B\int((\hbar\omega/k_B T)/exp(\hbar\omega/k_B T) - 1)F(\omega)d\omega - F(T) \tag{14}$$

Furthermore, the lattice contribution to the heat capacity (C_v) can be obtained using:

$$C_v(T) = k_B\int((\hbar\omega/k_B T)^2\exp(\hbar\omega/k_B T)/[\exp(\hbar\omega/k_B T) - 1]^2)F(\omega)d\omega \tag{15}$$

The empirical Debye temperature (Θ_D), which is obtained by experimental data, indicates that at higher temperatures the modes begin to be excited, and below this value, the modes start to freeze. Considering Θ_D, we can obtain the following equation:

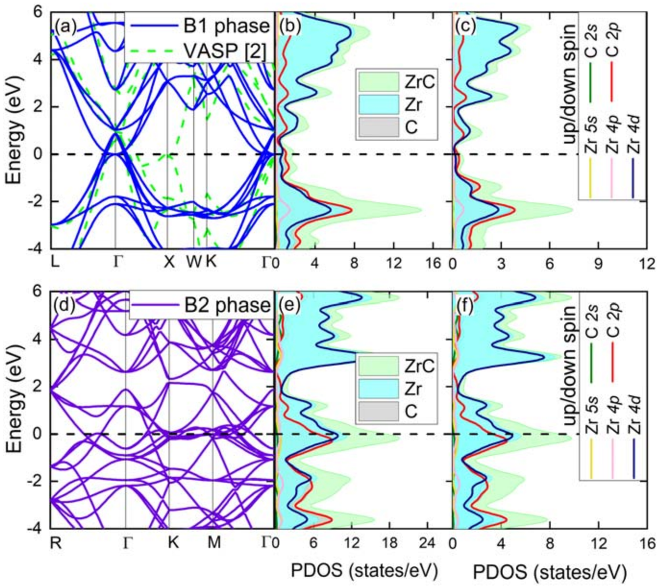

Figure 1. Electronic bands structure for the ZrC (a) B1 and (d) B2 phases, calculated with the GGA using the CASTEP code; for comparison, theoretical results obtained by using the VASP code [2] are shown. DOS and PDOS are shown for the (b) PM, (c) FM, A, C, and G-type AFM for the B1 phase. (e) PM, (f) FM, and G-type AFM PDOS for the B2 phase are also shown. The Fermi energy was set at zero.

$$k_B\Theta_D = \hbar\omega_D = \hbar c k_B \tag{16}$$

where ω_D is the maximum phonon frequency. Then, if $x = \hbar\omega/k_BT$, we can write the C_v as a function of the Debye temperature, as [39]:

$$C_v = 9nk_B(T/\Theta_D)^3\int_0^{\Theta D/T}(x^4e^x/(e^x - 1)^2)dx \tag{17}$$

When electromagnetic radiation strikes a material, it can be absorbed, reflected or transmitted; and the relative extent of these effects is directly dependent on the material. The frequency-dependent complex dielectric function was employed for the calculation of optical properties, and this is defined by:

$$\varepsilon(\omega) = \varepsilon_1(\omega) + i\varepsilon_2(\omega) \tag{18}$$

were the second term (equation (18)) was obtained from the occupied and unoccupied electronic states (data taken from the moment matrix) [35], which is represented by the following equation:

$$\varepsilon_2(\omega)) = 2e^2\pi/\Omega\varepsilon_0\sum_{\mathrm{k,v,c}}|\langle\psi_k{}^c|\ \mathrm{u}\cdot\mathrm{r}|\psi_k^v\rangle|^2\delta(E_k^c - E_k^v - \hbar\omega) \tag{19}$$

Where Ω represents the until cell volume, u is the polarization of the incident electric field and ψ_k^c and ψ_k^v are the wave functions for the conduction and valence bands, respectively. The first part of the equation (18) ($\varepsilon_1(\omega)$) can be obtained from the value of $\varepsilon_2(\omega)$, using the Kramers-Kroning transformation. In addition, the adsorption spectrum, the loss function, the reflectivity, and the refractive index were evaluated as in [35].

3. Results and discussion

3.1. Magnetic configurations

The electronic bands structure (EBS) allows to identify the electronic material's behavior (metal, semiconductor or insulator). The calculated EBS (this work) for the B1 phase shows a metallic compound. This behavior agrees with that found for the paths L–Γ and W—K–Γ, reported by Yang *et al* [2] (figure 1(a)) and calculated with the Vienna *Ab initio* Simulation Package (VASP) code; however, at point 'X' the two bands close to the E_F, calculated with the VASP code, differ. This may be due to the approximation and functionals taken into consideration since no significant changes in the partial and total densities of states (PDOS and DOS, respectively) are observed near the E_F. The EBS for the B2 phase (figure 1(d)), also defines a metallic compound.

The PDOS and DOS are shown for the different MCs (figures 1(b), (c), (e) and (f)). To model the B1 and B2 phases, the formal charges and spin channels were considered to generate the FM and the A, C, and G AFM initial magnetic types. Once the ground state of each system was reached, the DOS for the FE and the AFM cases shows the same states' contributions from the up and down spin channels. For the B1 and B2 phases (FE and the AFM cases), states' contributions from the up and down spin channels are the same. The B1 phase has a higher

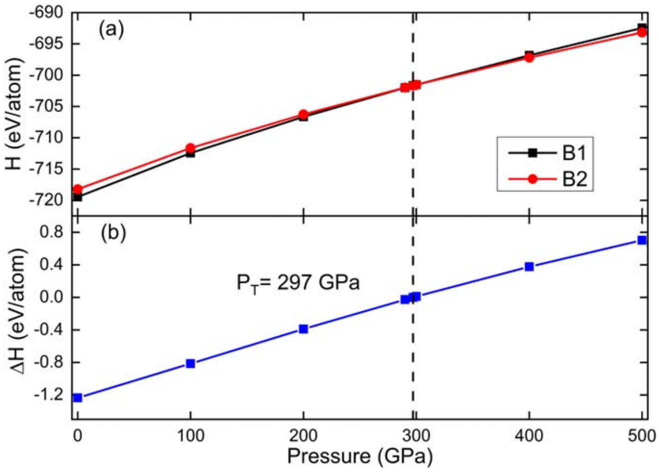

Figure 2. (a) Enthalpy for B1 (black) and B2 (red) phases, and (b) enthalpy difference (blue) between both phases, for ZrC under pressure.

contribution of states from C *2p*-orbitals between 0.3 and −4.0 eV; also, from Zr *4d*-orbitals around 6 and 0.3 eV (figures 1(b)–(c)). For the B2's valence band (VB) there is a higher contribution of states from C *2p*-orbitals, while for the conduction band (CB) the Zr *4d*-orbitals contribute the most (figures 1(e)–(f)).

From the criterion proposed in [40, 41], to determine the magnetic state through the calculated values for the 2^* Integrated Spin Density (2^* ISD) and the 2^*Integrated |Spin Density| (2^*I |SD|), it is possible to indicate that all the MCs (for both phases) are paramagnetic, because the values of 2^* ISD and 2^*I |SD| are zero for all cases. That criterion is supported by the fact that all MCs have associated the same total energy value, and contributions to PDOS (FM and AFM cases) from both spin channels are the same.

3.2. Thermodynamic stability and structural parameters

From the obtained enthalpy values (figure 2(a) and table 1) and the enthalpy difference between the B1 and B2 phases (figure 2(b)), as pressure is applied, it is possible to identify that the B1 phase is more stable than the B2 phase, at zero GPa; that agree with many other reported studies [4, 11, 42–46], and the behavior remains until the exerted pressure is more significant than 297 GPa. Then, the B2 phase becomes more stable; therefore, P_T was identified as the pressure where the transition from B1 to B2 occurs (figure 2(a)). That value is almost the same than those reported in references [11, 42, 43] but lower than those pressures reported in [4] (525 GPa) and [47] (358 GPa). These differences can be attributed to the different pseudo-potential used.

Among the calculated lattice parameter, volume, and enthalpy values, obtained for both phases as a function of the applied pressure (table 1), the *a* lattice parameter values agree with values reported in other works [4, 11, 42–46]: 4.075 Å for the B1 phase (at zero GPa) and 2.919 Å for the B2 phase.

The normalized lattice parameter and volume for ZrC exhibit discontinuities at P_T (figure 3(a)), which indicates a phase transition. For the B1 phase, from zero GPa to P_T, the *a* lattice parameter and the volume decrease 15% and 40%, respectively; then, from P_T to 500 GPa (B2 phase), those decrease 5% and 14%, respectively. Furthermore, from zero to 297 GPa, the Zr–C and Zr–Zr bond lengths decrease 15% (figure 3(b)) for the B1 phase. The Zr–C bond length increases abruptly by 6%, but the Zr–Zr bond length decreases by 13%. From P_T to greater pressures (B2 phase), the Zr–C and Zr–Zr bond lengths drop by 5%; this behavior indicates the stabilization of the structure.

3.3. Electronic properties

The bands structure provides information that allows to identify a system as conductor, semiconductor or insulator. It has been observed that the ZrC ceramic material has a metallic nature [5]. It does not change its metallic behavior due to the applied high pressure (figure 4). At zero GPa (B1 phase), the CB closer (CB-1) to the Fermi energy (E_F) has positive energy values only at the Γ point, while the VB closer to E_F (VB + 1) has a value of 0.4 eV at the Γ point (figure 4(a)). When the structure is subjected to 297 GPa (figure 4(b)), the CB valley moves to the top of the VB crest and, at P_T, the VB crest values vary from 1.0 (B1 phase) to 2.4 eV (B2 phase). On the other hand, the CB valley splits into two: one at 2.1 eV (between the Γ and X points) and the second at 1.1 eV, closer to the E_F, between the R and Γ points (figure 4(c)). The same trend is observed for the B2 phase at 500 GPa (figure 4(d)): the VB crest value increases until it reaches 2.9 eV, and the CB valley energy decreases to 0.8 eV.

Table 1. Structural parameters and enthalpy per atom (H atom^{-1}), calculated for ZrC under pressure.

Pressure (Gpa)	a (Å)	V(Å3)	H atom^{-1} (eV)
B1 phase			
0	4.705	104.158	−719.444
100	4.307	79.915	−712.449
200	4.111	69.473	−706.660
290	3.987	63.380	−702.007
297 (P_T)[a]	3.979	62.975	−701.662
300	3.975	62.804	−701.514
400	3.868	57.876	−696.819
500	3.781	54.057	−692.455
0 (Exp.)	4.694[b]		
0 (Exp.)	4.698[c]		
0 (Theo.)	4.706[d]		
0 (Theo.)	4.714[e]		
0 (Theo.)	4.930[f]		
0 (Theo.)	4.726[g]		
0 (Theo.)	4.698[h]		
B2 phase			
0	2.919	24.891	−718.208
100	2.649	18.596	−711.635
200	2.522	16.035	−706.270
290	2.444	14.601	−701.979
297(P_T)[a]	2.439	14.507	−701.661
300	2.439	14.470	−701.526
400	2.373	13.363	−697.191
500	2.322	12.517	−693.158
0 (Theo.)	2.946[d]		
0 (Theo.)	2.925[e]		
0 (Theo.)	2.945[g]		
0 (Theo.)	3.020[h]		

[a] Some transition (from B1 to B2) pressure values, reported from another theoretical works, are 289 [11], 303 [42], 358 [43], 525 [4] and 308 GPa [47].

[b] [44].

[c] [45].

[d] [11].

[e] [42].

[f] [46].

[g] [43].

[h] [4].

At the partial (per orbital), and total densities of states (PDOS and DOS, respectively; figure 5) for ZrC, it is possible to observe a states' bunching at −2.3 eV (VB, at zero GPa). This contribution is mostly provided by the C *2p*-orbitals (52%) and Zr *3d*-orbitals (38%). Three areas at the CB are notable: the highest states' bunching, between 4 and 5 eV, followed by a peak around 2.6 eV and another at 1.1 eV. These electronic states come from the Zr *4d*-orbitals, which contribute 80%, and the C *2p*-orbitals which contribute 17% (figure 5(a)). Furthermore, the B1 phase's electronic states at the DOS (297 GPa) are localized mostly at four zones around −2.7, 4.0, 5.0, and 5.3 eV (figure 5(b)). The VB peak located at −2.7 eV is reduced by around 51%, with respect to that of the DOS at zero GPa (figures 6(a) and (b)). Likewise, the states' density at the CB, between 4 and 5 eV, was reduced by 50% and located at 5.3 eV. This redistribution is observed on the PDOS: contributions from C (41% from C *2p*-orbitals) and Zr (47% from the Zr 4d− and 10% from the Zr 4p-orbitals) to the VB; being the C 2p-orbitals and the Zr *4d*-orbitals closer to the E_F. Moving away from E_F (around 5.6 eV), the contribution of the Zr 3*d*-orbitals increases to 67%, and the C *2p*-orbitals' contribution decreases to 22%. At P_T the structure changes to the B2 phase (figure 5(c)); then, the DOS accumulation at −2.7 eV (VB) moves to −0.5 eV (figures 5(b) and (c)). Closer to E_F, the states' concentration is provided by the C *2p*-orbitals (55%), Zr *4d*, and Zr *5s*-orbitals by 35 and 10%, respectively. For the CB, at 5 eV, the Zr 4d (56%) and 5 s (14%) orbitals contribute the most. The accumulation of states at the VB decreases by 18%: 46% from C *2p*-orbitals and 39% from Zr *4d*-orbitals (figure 5(d)). On the other hand, the highest accumulation at the CB decreases by 54%; in this zone, the largest contribution comes from the Zr *4d* and *5s*-orbitals by 71% and 15%, respectively. The decrease of the

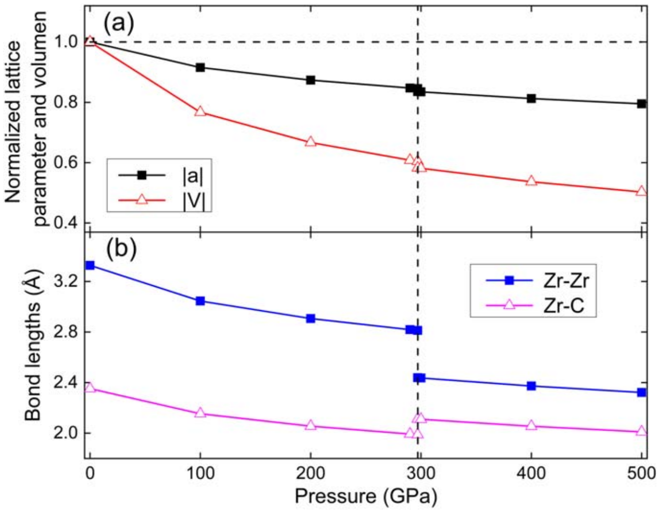

Figure 3. (a) Normalized volume (red) and lattice parameter (black), and (b) variation of the bond length for the B1 and B2 phases for ZrC under pressure.

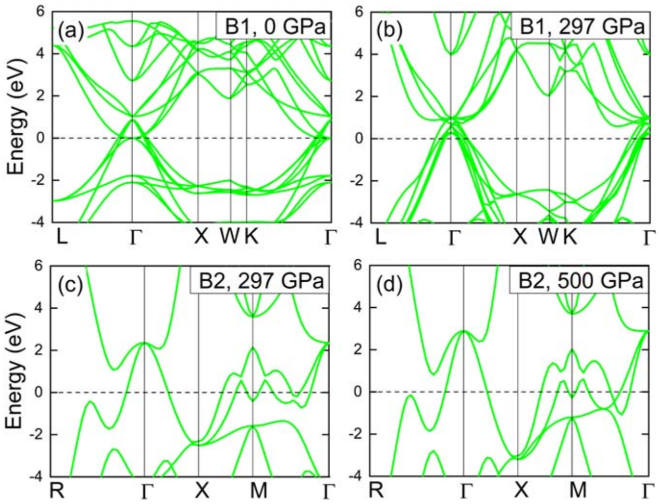

Figure 4. Electronic band structure for ZrC, at (a) zero, and (b) 297 GPa for the B1 phase; also, at (c) 297 and (d) 500 GPa for the B2 phase. The Fermi energy is set at 0 eV.

concentration of states at the DOS indicates a greater distribution of states along the CB and the VB; in addition, the displacement of the concentration of states from the VB to values closer to the E_F from the C *2p*-orbital is observed.

The Mulliken population analysis and the electron density difference could help to understand the interaction between the atoms in the system; both were computed (figure 6(a)). It is observed that, at zero GPa (figure 6(b)), the C atoms gain a charge of -0.79 |e| while the Zr atoms exhibit a charge of 0.79 |e|, indicating a strong coulombic interaction (ionic character). According to other works [2, 44], for which this behavior manifests, a covalent-ionic bond has been reported. C atom's charge increases to -0.8 |e|, at 100 and 200 GPa, indicating that there is a greater interatomic force at these pressures. At 297 GPa, the C atoms charge decreases to 0.79 |e|; there is also a charge gain at the Zr–C bond (figure 6(c)) compared to charges at zero GPa; this is supported by the decrease of the bond lengths and the greater states distribution around E_F described for the PDOS. An abrupt 7.6% decrease of the C atoms' charge is observed when the phase changes to B2 at P_T. Compared to the phase B1, the B2 phase exhibits a charge accumulation between Zr atoms and a charge loss between the C atom and their Zr neighboring atoms (figure 6(d)); these gain/loss of charge explain the abrupt change of the Zr–Zr (decrease) and Zr–C (increment) bond lengths. The 0.73 |e| is maintained from P_T to 500 GPa; however, there is a charge increase around the C atom (figure 6(e)), indicating a greater contribution of

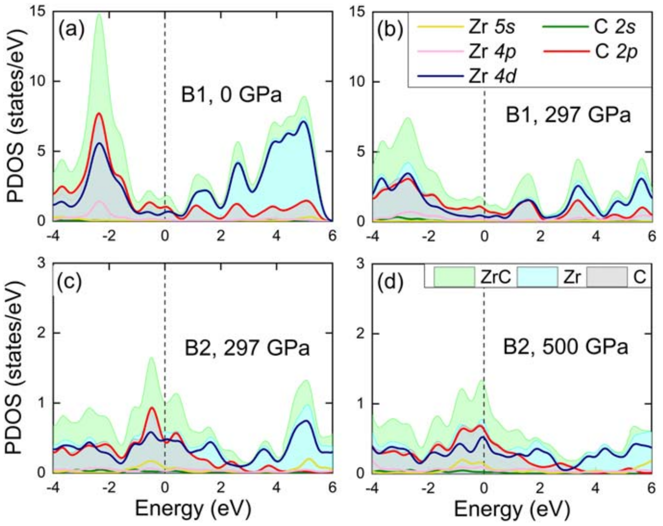

Figure 5. Total DOS (full green) and PDOS for Zr (full blue) and C (full gray) atoms. Contributions from the Zr *s* (yellow line), *p* (pink line), and *d* (dark blue line) orbitals, as well as from the C *s* (dark green line), and *p* (red line) orbitals, are shown for: the B1 phase, at (a) 0 and (b) 297 GPa, and for the B2 phase, at (c) 297 and (d) 500 GPa.

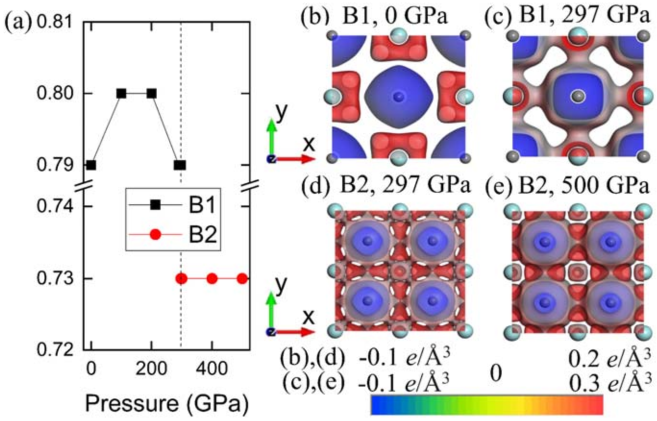

Figure 6. (a) Mulliken population analysis for the C atoms in the ZrC compound. Electron density difference between atoms for the B1phase, at (b) zero GPa and (c) 297 GPa, and for the B2 phase at (d) 297 GPa and (e) 500 GPa. The magnitude of the charge for C and Zr atoms is the same, but the signs are opposite. At the right bottom is shown the charge scale for (b)–(e). Gray and light blue spheres represent the C and Zr atoms, respectively.

the *2p*-orbitals around E_F and, consequently, the decrease of the Zr–C bond length. For the case of charge increase and bond decrease between Zr atoms, they cause an increase in the distribution of their *4d*-orbitals.

The E_{coh} is a measure of the energetic stability of a system, and is defined as the electrostatic energy that holds all atoms together to build up a structure. The ZrC stability diminishes as the applied pressure increases (figure 7), and this behavior follows its enthalpy increase. The cohesive energy decreases 35% for the B1 phase, when the pressure goes from zero to 297 GPa. There is an abrupt energy change (19%) at P_T, reaffirming the transition from the B1 phase to the B2 phase. From 297 to 500 GPa, a similar cohesive energy diminishing trend is observed; the energy is reduced by 50%.

3.4. Mechanical properties

The ZrC fulfillment of the mechanical stability criteria (equations (3)–(6)) is essential for the correct prediction of the structures' mechanical properties under pressure. The calculated elastic constants' values (table 2) for ZrC, at zero GPa, are in good agreement with results from theoretical [5] and experimental [48] studies on the ZrC. The C_{11} and C_{12} values of the elastic constants for ZrC gradually increase, up to 297 GPa; for the C_{44} case, a slight decrease is observed. It is evident a transition from the B1 phase to the B2 phase, since the C_{11} value decreases up to 75%; at the same time, the C_{12} and C_{44} values increase 2.5 and 3 times, respectively (figure 8(a)). At 400 GPa, C_{12} decreases 24%, C_{11} rises 4 times up the initial value, while C_{44} only changes 9%. The reported experimental

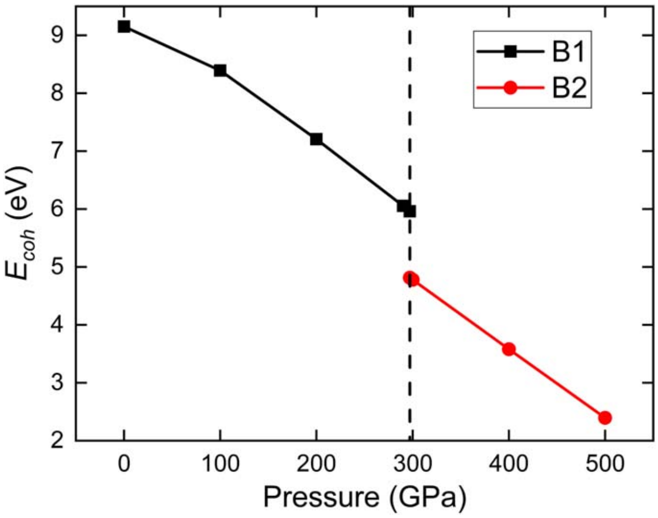

Figure 7. Cohesive energy for the crystalline ZrC, under pressure, for the B1 (black) and B2 (red) phases.

Table 2. Elastic constants (C_{ij}), bulk modulus (B_0), Shear and Young's moduli (G and Y); their values are in GPa units.

Pressure (GPa)	C_{11}	C_{12}	C_{44}	B_0	G	Y
B1						
0	460	104	152	223	162	391
100	1211	250	187	570	276	714
200	1700	466	172	877	296	798
290	2012	619	126	1083	271	751
297	2046	630	122	1102	269	747
0 (Exp.) [46]	472	99	159	223	170	406
0 (Theo.) [5]	468	102	148	224	161	390
B2						
297	514	1414	355	1114	643	1620
300	534	1416	361	1122	681	1700
400	2004	1083	387	1390	415	1120
500	2399	1301	566	1667	559	1510

B_0 at zero GPa has a value of 223 GPa [49], which is consistent with our results (table 2). B_0 holds a linear increase up to 297 GPa; moreover, G and Y exhibit similar behavior since these show a maximum value at 200 GPa and decrease slightly at P_T (figure 8(b)). When the ZrC structure changes from the B1 to the B2 phase, an increase (of 1%) is observed for B_0, while G and Y increase more than twice their values. B_0 shows the same behavior for both phases (B1 and B2); in contrast, other modules have a more irregular behavior. G and Y increase 6% and 5%, respectively, from P_T to 300 GPa; but decrease to 39% and 34% at 400 GPa. However, both moduli increase 35% their values when the applied pressure reach 500 GPa.

The Pugh's ratio (K) values exhibit the brittleness of the B1 phase, at zero GPa, as well as their turning to ductile with increasing pressure (figure 9(a)). The B2 phase, is brittle at pressures of 297 and 300 GPa, but ductile at 400 and 500 GPa. The B1 phase is ionic-covalent, at zero and 100 GPa, while it is metallic at 200 and 297 GPa (figure 9(a)). Additionally, the calculated Poisson's ratio (ν) agrees with the electronic properties described. On the other hand, the B2 phase is ionic-covalent at 297 and 300 GPa, but metallic for the remaining pressures. Then, the material is brittle at low pressures, due to the high interatomic forces involved to bond the atoms. Furthermore, as the pressure increases, the bonds weaken, the charges are delocalized; however, accumulating states near the E_F make the material more ductile. On the other hand, H_V values gradually decrease until 59% at 297 GPa (B1 phase); however, when the phase changes to B2, H_V increases 5 times its value (figure 9(b)). As could be seen at the rest of the mechanical properties, from P_T, the material stabilizes.

3.5. Vibrational properties

The PD, associated to the ZrC under pressure, was investigated at high symmetry points and along the lines that connect these points (figure 10). The L–Γ, Γ–X, X–W, W–K and K–Γ lines are along [111], [100], [−1 2 0], [−1 1

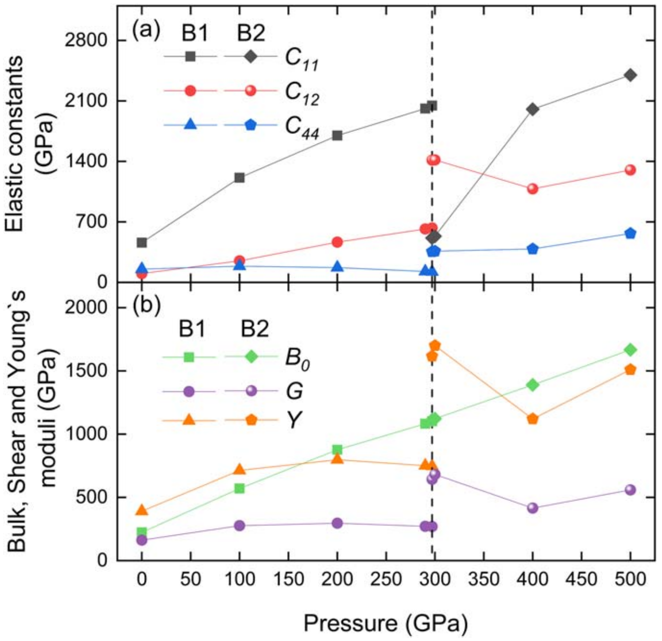

Figure 8. (a) Elastic constants values (C_{ij}) and (b) bulk (B_0), shear (G), and Young's (Y) moduli for the modeled ZrC under pressure.

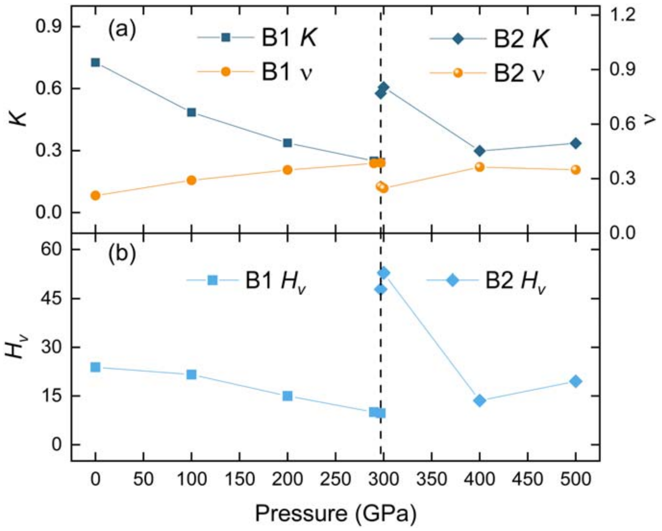

Figure 9. (a) Pugh's ratio (K), Poisson's ratio (ν), and (b) Vickers hardness (H_V) for the modeled ZrC under pressure.

0] and [110] directions, respectively. At zero GPa, the PD exhibits 24 branches: 21 optical and 3 acoustic (figure 10(a)). No imaginary phonon frequencies or soft phonon modes were observed at the whole BZ, indicating dynamical stability, and agreeing with another reported studies [36, 50]. The optical mode frequencies at the Γ point are 6.78, 7.88, 12.17, 13.32, and 15.66 THz. The dynamical stability of the B1 phase is backed by the PD at 297 GPa (figure 10(b)). The branches occupy a wider interval at the low-frequency region (LFR) but are localized at a compressed one at the high-frequency region (HFR), as the applied pressure rises. Frequencies increase at the Γ point when the pressure reaches P_T. Frequencies of 6.79 and 10.67 THz are in the LFR; while 25.43, 26.30, and 27.95 THz are in the HFR. At 297 GPa, when occurs the transition to the B2 phase, the system is dynamically unstable due to negative frequencies in the acoustic modes. On the other hand, the frequencies of the optical mode approach each other to values of 22.7, 22.9, and 23.1 THz at the Γ point. ZrC is also unstable at 500 GPa; however, negative frequencies only occur along the Γ–M–X–Γ path (figure 10(d)).

The calculated partial phonon density of states (PPDOS), for ZrC at zero GPa, is divided into two frequency regions (figure 11(a)): the LFR (from 1 to 9.9 THz) and the HFR (from 12 to 20.1 THz). The Zr atoms' vibrations contribute to the phonon branches in the LFR, with a maximum peak at 6.4 THz; meanwhile, the C atoms'

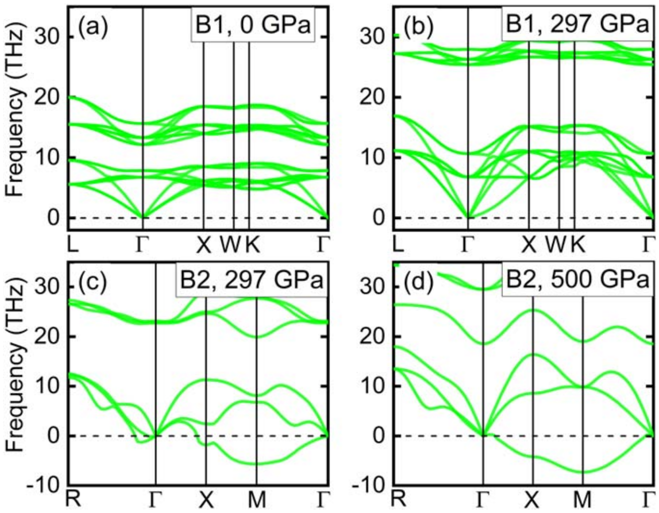

Figure 10. Phonon dispersion curves for the B1 phase of the ZrC at (a) zero GPa and (b) 297 GPa. Also, the B2 phase's phonon dispersion can be seen for (c) 297 GPa and (d) 500 GPa.

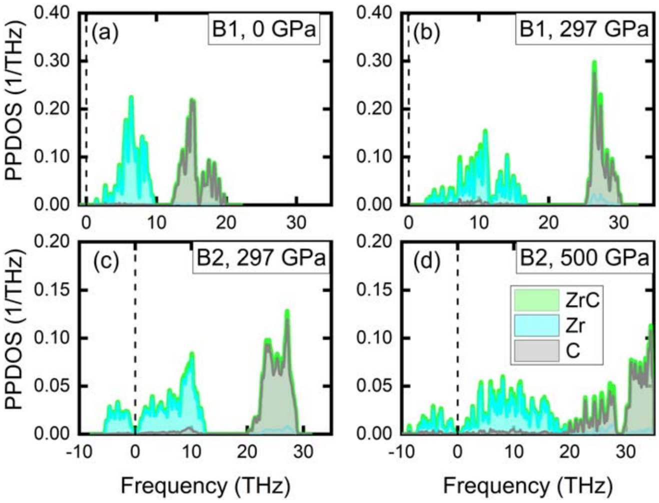

Figure 11. Partial, and total phonon density of states for the ZrC compound (green), and the Zr (blue), and C (gray) atoms.

vibrations contribute to the HFR, where two maximum peaks are located at 15.0 and 15.3 THz. Furthermore, the phonon's bandgap between the HFR and the LFR is of 2.1 THz. At 297 GPa (figure 11(b)), the LFR is 67% wider, with a maximum at 12 THz; however, the HFR decreases to 69%, with a maximum located at 26.5 THz. Also, the forbidden phonon band increases almost four times. At P_T, from the B1 to the B2 phase (figure 11(c)), LFR ranges from −5.8 THz to 12.8 THz and HFR from 19.8 to 29.3 THz; the forbidden phonon band decreases 12%. The maximum peaks are located at 10.1 THz, for LFR, while there are at 23.4 and 27.1 THz for HFR. At 500 GPa (figure 11(d)), unlike the other pressures, Zr and C atoms contribute to the vibrations in the LFR; these vibrations intersect at 20 THz. On the other hand, the C atom's vibrations contribute to the HFR. Furthermore, the maximum peak for the LFR is at 8 THz and the corresponding for the HFR is at 34.4 THz, contributed by Zr and C vibrations, respectively. The bond lengths decrease, as the pressure increases, generating a vibration unbalance on each atom. C atoms increase their frequency more than the Zr atoms, because the atomic C mass is smaller than the Zr atomic mass. Then, vibrations are an indicator that neighboring chains between C atoms cause the negative frequencies in the G–X, X–M and M–G lines, along the [010], [2 1 0] and [110] directions, respectively; while the neighboring chains between C and Zr atoms cause the negative frequencies in the R–G line along the [111] direction.

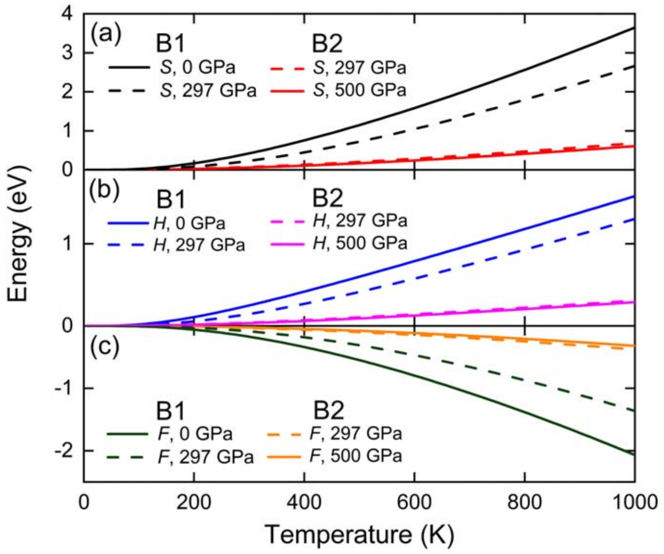

Figure 12. (a) Entropy (S), (b) enthalpy (H), and (c) Helmholtz free energy (F) for the ZrC compound, under pressure.

3.6. Thermodynamical properties

The PPDOS is necessary to evaluate the dependence of the entropy (S), enthalpy (H), Helmholtz free energy (F), heat capacity (C_v), and Debye temperature (Θ_D) of a crystal in the quasi-harmonic Debye model [39], on temperature. Then, the phonon contribution to the F, H, S, and C_v at temperatures from 0 to 1000 K is shown at figure 12. The calculated zero-point energies (B1 phase) are 0.5383 and 0.9330 eV, at 0 and 297 GPa, respectively; these values agree with those reported in [51]. For the B2 phase, the obtained zero-point energies are 0.1929 and 0.2386 eV, at 297 and 500 GPa, respectively.

The calculated values for S and H increase continually (figures 12(a) and (b)), as temperature increases; this trend also was reported in [36]. However, those values drop at the transition (from B1 to B2) driven by the applied pressure. The entropy associated to B2 is smaller than that associated to B1 (figure 12(a)), notoriously at high temperatures; this fact was reported, also, in [52]. In other words, the B2 phase lattice order is better than that for the B1 phase under pressure at high temperatures. On the contrary, the F gradually decreases with increasing temperature, but increases under pressure (figure 12(c)), after the transition. This result indicates that the B1 phase is more stable than the B2 phase at high temperatures.

The C_v increases with the temperature but decreases abruptly at the transition (from B1 to B2, figure 13(a)). First, when the temperature is lower than 500 K, C_v increases rapidly obeying the well-known Debye model; later, for temperatures higher than 500 K, C_v increases slowly with the temperature and tend to the asymptotic limit (so-called the Dulong-Petit limit) of 46.4 cal cell^{-1} K, which agrees with many other reported studies [52–54]. On the other hand, for the B1 phase at room temperature, C_v depends on the pressure; when pressure varies from 0 to 297 GPa, C_v changes from 24.6 cal cell^{-1} K to 5.9 cal cell^{-1} K. At zero GPa (B1 phase), the zero Θ_D is 329.5 K (figure 13(b)). As the temperature varies from 0 to 1000 K, the Θ_D increases quickly and then reach a constant value at about 286 K. At 297 GPa, the zero Θ_D is 0 K, it increases dramatically at 15 K; however, it decreases and stabilizes as a constant at 407 K. For the B2 phase, the zero Θ_D are 198.5 and 282 K for 297 and 500 GPa, respectively; Θ_D increases rapidly up to room temperature and increases steadily from this point.

3.7. Optical properties

The absorption coefficient provides information to know how far the light, with a specific wavelength, penetrates a material before it is dissipated; therefore, this coefficient provides helpful information on the ideal efficiency for solar energy conversion [55]. The ZrC at zero GPa [56] exhibits two absorption peaks (at 10.3 and 31.2 eV, figure 14(a)) in the UV region [53]; besides, the peaks in the visible region are very weak. Once the pressure reaches the value 297 GPa, the absorption in the UV region increases: four peaks are found at 11, 16.1, 32.3, and 34.8 eV. Above P_T, the absorption by the B2 phase slightly decreases, in a region between 11.5 and 40.6 eV. The UV absorption region grows at 500 GPa, ranging from 7.6 to 42.2 eV, and the absorption values also increase. Therefore, at high pressures, ZrC increases the photon adsorption range, indicating that it could be used for optical and optoelectronic devices in the UV region.

On the other hand, being the reflectivity the capability of a surface to reflect the incident radiation [57], it was found that the highest reflectivity peak is in the infrared zone (at 0.01 eV, value of 0.99 for zero GPa,

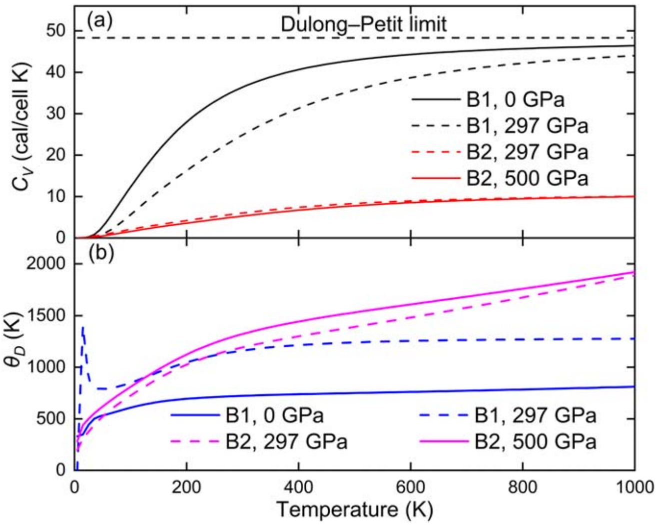

Figure 13. Heat capacity (C_v) and Debye temperature (Θ_D), at constant volume, for the ZrC compound under pressure.

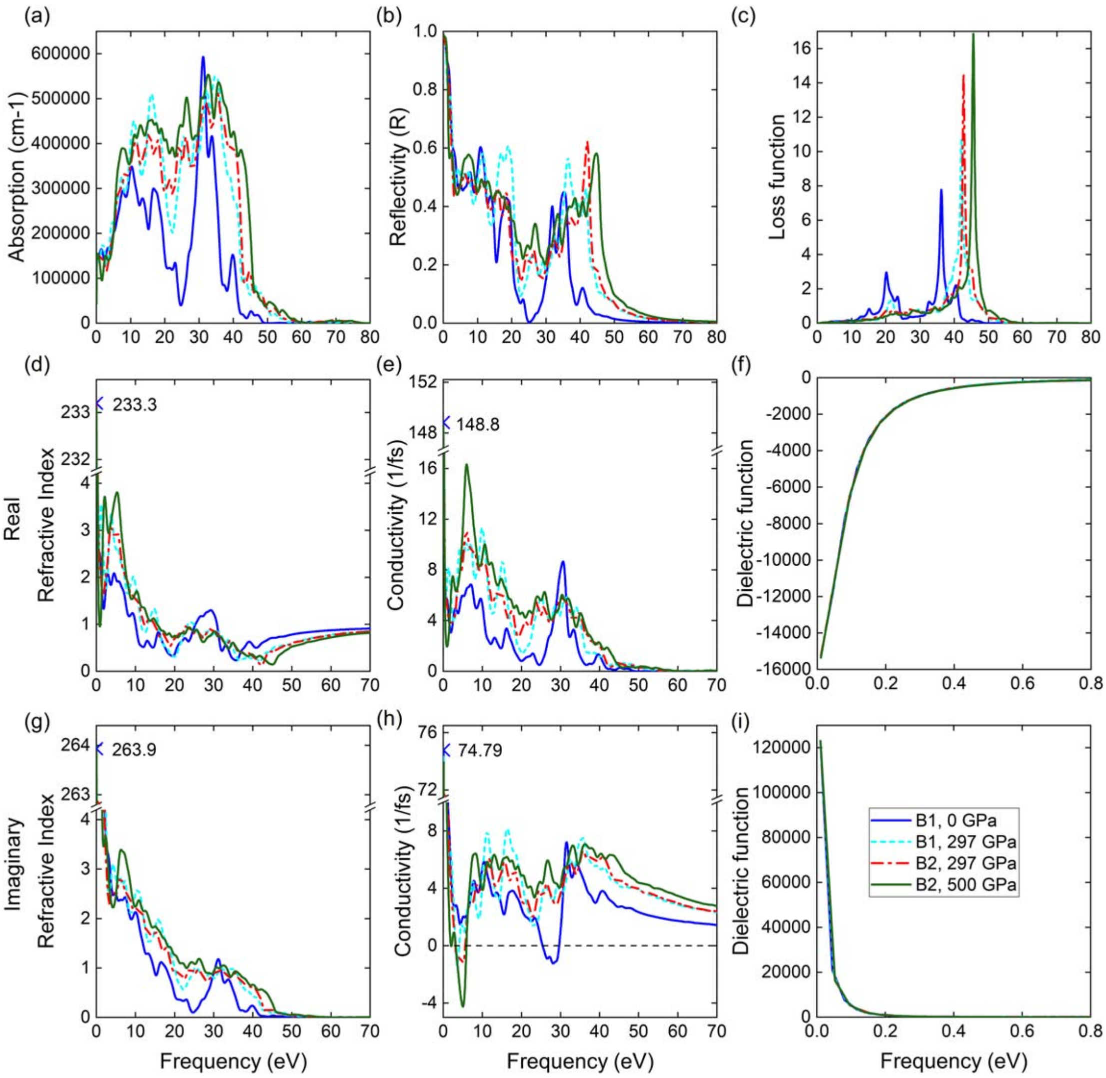

Figure 14. Optical parameters for the B1 phase of the ZrC at: zero GPa (blue line) and 297 GPa (cyan dashed line). Also, information for the B2 phase is shown for: 297 GPa (red dashed line) and 500 GPa (green line). Graphs for (a) absorption, (b) reflectivity, (c) loss function, (d) real and (g) imaginary refractive index, (e) real and (h) imaginary conductivity, (f) real and (i) imaginary dielectric function are shown.

figure 14(b)); but the reflectivity decreases considerably, reaching a minimum at 25.1 eV, in the UV zone. Only two great peaks were found for higher frequencies: at 31.8 eV (value of 0.4) and 35.3 eV of (value of 0.45). From 0 to 8 eV, the calculated reflectivity agrees with that reported by J F Alward *et al* [58]. There is a reflectivity decrease, at low frequencies, for the B1 phase at 297 GPa; however, the reflectivity increases at the UV zone, with a valley at 22.6 (0.1) between two peaks at 18.9 eV (0.61) and 36.4 eV (0.57). For the B2 phase, the reflectance increases, starting from the infrared zone to frequencies of 42.1 eV (value of 0.62) and 45.1 eV (value of 0.18) for pressures of 297 GPa and 500 GPa, respectively. The high reflectivity values at low frequencies reveal a refractory material; and, as the pressure increases,the possibility of use this as a coating material increases.

The energy loss function is a dielectric parameter that describes the collective excitations produced by the swift charges. The frequency at the maximum energy loss is known as the bulk plasma frequency (ω_p) and occurs at $\varepsilon_1 = 0$ and $\varepsilon_2 < 1$ [59]. For frequencies below ω_p, the materials are reflective; whereas, above this frequency, the material is transparent [60]. The maximum bulk plasma frequencies (figure 14(c)) were found at 36.3 and 42.1 (B1 at 0 and 297 GPa, respectively), and 42.7 and 45.6 eV (B2 at 297 and 500 GPa, respectively). The peak for the bulk plasma frequency, at zero GPa (20.1 eV), is between those reported by F Espinosa *et al*: 19 eV at 2001 [61] and 22.2 eV at 2002 [62]. The shift of ω_p to higher frequencies, and the energy loss function values, depend on the applied pressure rise.

An incident wave on a material could be refracted or bent, and the wavelength variation amount is quantified by means of the refraction index; their real and imaginary (extinction coefficient) parts indicate the phase velocity and the attenuation amount, respectively [57]. At zero GPa, there is a higher phase velocity in the infrared spectrum (0.01 eV), decreasing considerably at higher frequencies (figure 14(d)); however, there are two peaks within the visible (2.9 eV) and UV (4.5 eV) regions. At 297 GPa, the B1 phase maintains the highest phase velocity in the infrared region, but there is an 65% increase of the phase velocity and two peaks shift to frequencies of 1.2 and 3.3 eV. The B2 phase's peaks show another change at 3.8 and 5.3 eV frequencies, at the phase transition. For 500 GPa, there is another 24% increase for these two peaks and a change at 2.1 and 5.2 eV frequencies.

On the other hand, the greatest wave attenuation (figure 14(g)) made by the ZrC at zero GPa was found in the infrared region, followed by another in the visible region. At the UV region, waves are less attenuated, except those at 31.2 eV; those of 42 eV are almost nil. At the pressure of 297 GPa, attenuation increases around 40% in the UV region; and a plateau was formed between 25.5 and 34.5 eV. Additionally, there is almost no attenuation at 50.2 eV. When phase changes to B2 at P_T, the attenuation of waves decreases as it was observed for B1, but the decreasing trend occurs without fluctuations. At 500 GPa, attenuation increases 20% if it is compared to that at 297 GPa.

The optical conductivity (or photoconductivity) is the optoelectronic phenomena which increases the electrical conductivity, as a result of the photons' absorption by the electrons, at the occupied states and the excitement of those into unoccupied states [55]. From the real and imaginary parts of the studied ZrC's photoconductivity (figures 14(e) and (h), respectively) was found that photoconductivity is higher in the infrared region, indicating the metallic nature of the ZrC [63]. The real part of the conductivity (at zero GPa) decreases after the infrared region, except for two peaks in the UV region (7 and 30.6 eV). The obtained peak at 3.1 eV has been reported in other works [58, 64], while the peak at 7 eV is close to that reported by A Delin *et al* (6.5 eV) [65]. At 297 GPa, the conductivity after the infrared region increases by approximately 60%; however, our results are larger by 26% and 50%, respectively, and shifted to frequencies of 9.9 and 31.8 eV. Once the compound changes to the B2 phase, the first peak shifts to 5.9 eV, and the conductivity steadily decreases having four intermediate peaks between 25 and 40 eV. At 500 GPa, only the first peak was found, at 5.9 eV and increased 45%. Regarding the imaginary part (at zero GPa), two peaks are observed in the UV region (10.4 and 31.5 eV) and a valley (28.1 eV) between these. Three peaks (11.2, 16.3 and 35.6 eV) are formed when pressure is 297 GPa, and the valley moves to the visible region (3.6 eV). Above P_T, for the B2 phase at 297 GPa, there are a conductivity reduction (20%), a slight displacement of the three peaks (11.7, 15.6, and 35.7 eV) and the formation of two valleys (3.6 and 5.1 eV) with negative values. At 500 GPa, a stable conductivity is noted from 8.5 to 43 eV and a valley at 5 eV.

The dielectric function provides information about the effects of the energy loss and the polarizability of a material while an electric field passes through it: the real part $\varepsilon_1(\omega)$, indicates the polarization extent and the imaginary part $\varepsilon_2(\omega)$ its absorption (equation (19)). The material is transparent if $\varepsilon_2(\omega) = 0$ and absorption begin when $\varepsilon_2(\omega) \neq 0$ [66]. At low frequencies, $\varepsilon_1(\omega)$ exhibits negative values (figure 14(f)) and, passing through the visible and UV zones, exponentially tends to zero. This behavior is the same for all the studied pressure range and the two phases. In addition, the obtained results show a zero upward crossing at 20.2 eV, which is similar to that reported by F Espinosa *et al* (19.4 eV) [62]. This crossover indicates a well-defined plasmon at the dominant peak observed by means of the loss function.

Regarding the imaginary part of the dielectric function (figure 14(i)), the behavior is the opposite of that for the real part; the former tends to zero as the frequency increases. This behavior implies that the ZrC, at high frequencies, becomes almost transparent with very little absorption; and this agree with the loss function. Other works, also, verify the well-defined shape of the $\varepsilon_2(\omega)$ curve [58, 64].

4. Conclusions

We have performed *ab-initio* calculations, based on the DFT, to study the structural, electronic, mechanical, vibrational, thermodynamical, and optical properties of the ZrC, under high pressure, for the rock salt (B1) and CsCl (B2) structures. The ZrC system shows a paramagnetic behavior at zero GPa. This B1 system is structural, thermodynamical, energetical, and dynamically stable; however, it is less stable as the pressure increases. A phase transition (from B1 to B2) was identified: at the pressure 297 GPa (P_T); above this pressure, the system is dynamically unstable.

The lattice parameters and volume decrease as pressure increases. The calculated lattice parameters, electronic bands structure, phonon dispersion curves, elastic, thermodynamic, and optical values are in good agreement with experimental and theoretical results published elsewhere for the B1 phase. The band structure, DOS, and electron density difference show that the B1 and B2 phases are metallic in the studied pressure interval.

The Poisson's ratio indicates that the ZrC has ionic-covalent bonds, and, as the pressure increases, the bond lengths decrease, favoring an increase of the C2p-orbitals near the EF. Pugh's ratio and Vickers hardness indicate that ZrC is a ceramic material (hard and brittle) and tend to be ductile under pressure. C atoms' vibrations contribute to HFR while Zr atoms' vibrations impact the LFR. As pressure increases, the phonons' band gap decreases; additionally, at 500 GPa, the C and Zr atom's vibrations contribute to the LFR. S, H, and θ_D values increase as the pressure increases while those for F and C_v decrease. This compound presents its highest mechanical resistance $T > 356°$ K and the maximum thermal absorption (46.4 cal cell^{-1}) $T > 638°$ K but when pressure is applied, these are found at $T > 1000°$ K and the máximum termal absorption decrease to 46.4 cal cell^{-1}. ZrC is a refractive material below 36.3 eV and is transparent above this frequency but increases to 45.1 eV as it increases to 500 GPa; it has associated a high phase velocity, wave attenuation and photoconductivity in the infrared interval and it has a defined plasmon in the UV region. In addition, ZrC is a good coating material and a photon detector in the UV region. Also, it was observed a shift of the frequencies towards higher values and increments of the values for the optical properties, as the pressure increases.

Acknowledgments

H Muñoz, J E Antonio, and J M Cervantes want to acknowledge the support from CONACYT and BEIFI-IPN. J L Rosas-Huerta acknowledges the postdoctoral scholarship SECTEI/098/2022 granted by Secretaría de Educación, Ciencia, Tecnología e Innovación de la Ciudad de México. This work was partially supported by the projects IPN-SIP 20201114, 20210203 and 20220567, and the UNAM-DGAPA-PAPIIT Program under Grants IN101421, IA105121 and IN100222. Calculations were done using resources from the Supercomputing Center DGTIC-UNAM.

Data availability statement

All data that support the findings of this study are included within the article (and any supplementary files).

ORCID iDs

H Muñoz https://orcid.org/0000-0001-8213-1466
J E Antonio https://orcid.org/0000-0001-8136-3521
J M Cervantes https://orcid.org/0000-0003-3714-1774
M Romero https://orcid.org/0000-0003-3363-757X
J L Rosas-Huerta https://orcid.org/0000-0002-8870-0313
E P Arévalo-López https://orcid.org/0000-0001-5513-2623
E Carvajal https://orcid.org/0000-0001-5107-3400
R Escamilla https://orcid.org/0000-0002-6876-0351

References

[1] Gubanov V A, Ivanovsky A L and Zhukov V P 1994 Electronic structure, chemical bonding and properties of binary carbides *Electronic Structure of Refractory Carbides and Nitrides* (Cambridge, New York: Cambridge University Press) pp 18–57

[2] Yang X Y, Lu Y, Zheng F W and Zhang P 2015 Mechanical, electronic, and thermodynamic properties of zirconium carbide from first-principles calculations *Chin. Phys. B* **24** 116301

[3] Singh A, Aynyas M and Sanyal S P 2009 Phase transition and high pressure behavior of Zirconium and Niobium carbides *Cent. Eur. J. Phys.* **7** 102–7

[4] Srivastava A, Chauhan M and Singh R K 2011 High-pressure phase transitions in transition metal carbides XC (X = Ti, Zr, Hf, V, Nb, Ta): A first-principle study *Phase Transit.* **84** 58–66

[5] Chauhan M and Gupta D C 2013 Electronic, mechanical, phase transition and thermo-physical properties of TiC, ZrC and HfC: High pressure computational study *Diam. Relat. Mater.* **40** 96–106

[6] Riedel R 2000 Properties of important transition metal carbides *Nitrides, and Carbonitrides Handbook of Ceramic Hard Materials* **1** 224–52

[7] Hantanasirisakul K *et al* 2020 Evidence of a magnetic transition in atomically thin Cr2TiC2TX MXene *Nanoscale Horiz* **5** 1557–65

[8] Cao R, Zhang J, Wang W, Hu Q, Li W, Ruan W and Ao H 2017 Synthesis and luminescence properties of CaSnO3:Bi3 + blue phosphor and the emission improvement by Li + ion *Luminescence* **32** 908–12

[9] Escamilla R, Muñoz H, Antonio J E, Arévalo-López E P, Rosas-Huerta J L and Romero M 2021 Phase transition and mechanical, vibrational, and electronic properties of NbC under pressure *Physica B Condens Matter* **602** 412594

[10] Abdel Rahim G P, Rodriguez J A and Moreno-Armenta M G 2017 First principles study of the structural, electronic, and magnetic properties of ZrC *Solid State Phenomena* **257** 211–5

[11] Ivashchenko V I, Turchi P E A and Shevchenko V I 2013 Phase transformation B1 to B2 in TiC, TiN, ZrC and ZrN under pressure *Condens. Matter Phys.* **16** 33602

[12] Hao A, Zhou T, Zhu Y, Zhang X and Liu R 2011 First-principles investigations on electronic, elastic and thermodynamic properties of ZrC and ZrN under high pressure *Mater. Chem. Phys.* **129** 99–104

[13] Hohenberg P and Kohn W 1964 Inhomogeneous electron gas *Phys. Rev.* **136** B864–71

[14] Search H *et al* 2002 First-principles simulation: ideas, illustrations and the CASTEP code *J. Phys. Condens. Matter* **14** 2717

[15] Clark S J, Segall M D, Pickard C J, Hasnip P J, Probert M I J, Refson K and Payne M C 2005 First principles methods using CASTEP *Z. Kristallogr.* **220** 567–70

[16] Perdew J P and Wang Y 1992 Accurate and simple analytic representation of the electron-gas correlation energy *Phys. Rev. B* **45** 13244

[17] Vanderbilt D 1990 Soft self-consistent pseudopotentials in a generalized eigenvalue formalism *Phys. Rev. B* **41** 7892–5

[18] Pfrommer B G, Côté M, Louie S G and Cohen M L 1997 Relaxation of crystals with the quasi-newton method *J. Comput. Phys.* **131** 233–40

[19] Monkhorst H J and Pack J D 1976 Special points for Brillouin-zone integrations *Phys. Rev. B* **13** 5188–92

[20] Bousquet E and Cano A 2021 Non-collinear magnetism & multiferroicity: the perovskite case *Physical Sciences Reviews* 2019007

[21] Zheng G, Ke S-H, Miao M, Kim J, Ramesh R and Kioussis N 2017 Electric field control of magnetization direction across the antiferromagnetic to ferromagnetic transition *Sci. Rep.* **7** 5366

[22] Fu H, Peng W and Gao T 2009 Structural and elastic properties of ZrC under high pressure *Mater. Chem. Phys.* **115** 789–94

[23] Romeo M and Escamilla R 2014 Pressure effect on the structural, elastic and electronic properties of Nb2AC (A=S and In) phases; *ab initio* study *Comput. Mater. Sci.* **81** 184–90

[24] Ersan F, Gökçe A G and Aktürk E 2016 Point defects in hexagonal germanium carbide monolayer: a first-principles calculation *Appl. Surf. Sci.* **389** 1–6

[25] Romero M and Escamilla R 2012 First-principles calculations of structural, elastic and electronic properties of Nb2SnC under pressure *Comput. Mater. Sci.* **55** 142–6

[26] Varshney D, Jain S, Shriya S and Khenata R 2016 High-pressure and temperature-induced structural, elastic, and thermodynamical properties of strontium chalcogenides *Journal of Theoretical and Applied Physics* **10** 163–93

[27] Romero M, Benitez-Rico A, Arévalo-López E P, Gómez R W, Marquina M L, Rosas J L and Escamilla R 2019 First-principles calculations of the structural, elastic, vibrational and electronic properties of YB6 compound under pressure *European Physical Journal B* **92** 1–7

[28] Antonio J E, Cervantes J M, Rosas-Huerta J L, Romero M, Escamilla R and Carvajal E 2021 Exposed surface and confinement effects on the electronic, magnetic and mechanical properties of LaTiO3 slabs *IEEE Trans. Magn.* **57** 1–4

[29] Antonio J E, Cervantes J M, Rosas-Huerta J L, Pilo J, Carvajal E and Escamilla R 2021 A first-principles investigation on the electronic and mechanical properties of 1T TiSe2 multilayers for energy storage *J. Electrochem. Soc.* **168** 030531

[30] Li J and Fan C 2015 Novel metastable compounds in the Zr–B system: An *ab initio* evolutionary study *Phys. Chem. Chem. Phys.* **17** 1180–8

[31] Perkowitz S 2018 Phonon Physics (https://britannica.com/science/phonon)

[32] Parlinski K, Li Z Q and Kawazoe Y 1997 First-principles determination of the soft mode in cubic ZrO2 *Phys. Rev. Lett.* **78** 4063–6

[33] Refson K, Tulip P R and Clark S J 2006 Variational density-functional perturbation theory for dielectrics and lattice dynamics *Phys. Rev. B* **73** 155114

[34] Lloyd-Williams J H and Monserrat B 2015 Lattice dynamics and electron-phonon coupling calculations using nondiagonal supercells *Phys. Rev. B* **92** 184301

[35] BIOVIA 2019 *Theory in CASTEP CASTEP Guide Materials Studio* **2019** 136–52

[36] Li H, Zhang L, Zeng Q, Ren H, Guan K, Liu Q and Cheng L 2011 First-principles study of the structural, vibrational, phonon and thermodynamic properties of transition metal carbides TMC (TM = Ti, Zr and Hf) *Solid State Commun.* **151** 61–6

[37] Cochran W 1959 Crystal stability and the theory of ferroelectricity *Phys. Rev. Lett.* **3** 412–4

[38] Mounet N and Marzari N 2005 First-principles determination of the structural, vibrational and thermodynamic properties of diamond, graphite, and derivatives *Phys. Rev. B* **71** 205214

[39] Ashcroft V N W and Mermin N D 1976 *Quantum Theory of the Harmonic Crystal Solid State Physics* **9** 458–61

[40] Goldsby J, Raj S, Guruswamy S and Azbill D D 2015 First-principle and experimental study of a gadolinium-praseodymium-cobalt pseudobinary intermetallic compound *J. Mater.* **2015** 1–9

[41] Rosas J L, León-Flores J, Escamilla R, Cervantes J M, Carvajal E, Verdín E and Romero M 2020 LDA + U study of the electronic and magnetic properties of the Sr2FeMo1-xNbxO6 compound *Mater Today Commun* **23** 101155

[42] Lv Z, Hu H, Wu C, Cui S, Zhang G and Feng W 2011 First-principles study of structural stability, electronic and elastic properties of ZrC compounds *Physica B Condens Matter* **406** 2750–4

[43] Qian J, Wu C and Gong H 2018 Phase transition, thermodynamic and elastic properties of ZrC *Transactions of Nonferrous Metals Society of China (English Edition)* **28** 2520–7

[44] Chinthaka Silva G W, Kercher A A, Hunn J D, Martin R C, Jellison G E and Meyer H M 2012 Characterization of zirconium carbides using electron microscopy, optical anisotropy, Auger depth profiles, X-ray diffraction, and electron density calculated by charge flipping method *J. Solid State Chem.* **194** 91–9

[45] Toth L 2014 *General Properties, Preparation, and Characterization Transition metal Carbides and Nitrides* (Amsterdam: Elsevier) 1–28

[46] Rathod N R, Gupta S K and Jha P K 2013 First-principles structural, electronic and vibrational properties of zinc-blende zirconium carbide *Solid State Commun.* **169** 32–6

[47] Rathod N, Gupta S K and Jha P K 2012 Dynamical stability and phase transition of ZrC under pressure *Phase Transit.* **85** 1060–9

[48] Chang R and Graham L J 1966 Low-temperature elastic properties of ZrC and TiC *J. Appl. Phys.* **37** 3778–83

[49] Chang R and Graham L J 1966 Low-temperature elastic properties of ZrC and TiC *J. Appl. Phys.* **37** 3778–83

[50] Guo Y, Chen J, Song W, Shan S, Ke X and Jiao Z 2021 Electronic, mechanical and thermodynamic properties of ZrC, HfC and their solid solutions studied by first-principles calculation *Solid State Commun.* **338** 114481

[51] Mellan T A, Aziz A, Xia Y, Grau-Crespo R and Duff A I 2019 Electron and phonon interactions and transport in the ultrahigh-temperature ceramic ZrC *Phys. Rev. B* **99** 094310

[52] Rathod N, Gupta S K, Shinde S and Jha P K 2013 First-principles investigation of thermophysical properties of cubic ZrC under high pressure *Int. J. Thermophys.* **34** 2019–26

[53] Zhu J, Zhu B, Qu J, Gou Q and Chen F 2009 Thermodynamic properties of cubic ZrC under high pressure from first-principles calculations science in China *Series G: Physics, Mechanics and Astronomy* **52** 1039–42

[54] Abdollahi A 2013 First-principle calculations of thermodynamic properties of ZrC and ZrN at high pressures and high temperatures *Physica B Condens Matter* **410** 57–62

[55] Naefa M J and Rahman M A 2020 First principles study of structural, elastic, electronic and optical features of the non-centrosymmetric superconductors SrMGe3 (Where M = Ir, Pt, and Pd) *International Journal of Material and Mathematical Sciences* **2** 16–28

[56] Rahaman M M *et al* 2019 Mechanical, electronic, optical, and thermodynamic properties of orthorhonmbic LiCuBiO4 crystal: A first-principles study *Journal of Materials Research and Technology* **8** 3783–94

[57] Roknuzzaman M, Hadi M A, Abden M J, Nasir M T, Islam A K M A, Ali M S, Ostrikov K and Naqib S H 2016 Physical properties of predicted Ti2CdN versus existing Ti2CdC MAX phase: An *ab initio* study *Comput. Mater. Sci.* **113** 148–53

[58] Alward J F, Fong C Y, El-Batanouny M and Wooten F 1975 Band structures and optical properties of two transition-metal carbides—TiC and ZrC *Phys. Rev. B* **12** 1105–17

[59] Roknuzzaman M and Islam A K M A 2012 Theoretical investigations of superconducting MAX phases Ti2InX (X = C, N) arXiv:1206.4514

[60] Hummel R E 2011 Optical properties of materials *Electronic Properties Of Materials* (Berlin: Springer) pp 227–335

[61] Espinosa-Magaña F, Duarte-Moller A, Martínez-Sánchez R and Paraguay-Delgado F 2001 Dielectric properties of ZrC by electron energy loss spectroscopy *Microsc. Microanal.* **7** 1152–3

[62] Espinosa-Magaa F, Duarte-Moller A, Martínez-Sánchez R and Miki-Yoshida M 2002 Electron energy loss spectroscopy of TiC, ZrC and HfC *J Electron Spectros Relat Phenomena* **125** 119–25

[63] Ali M A, Hossain M M, Uddin M M, Hossain M A, Islam A K M A and Naqib S H 2021 Physical properties of new MAX phase borides M2SB (M=Zr, Hf and Nb) in comparison with conventional MAX phase carbides M2SC (M=Zr, Hf and Nb): Comprehensive insights *Journal of Materials Research and Technology* **11** 1000–18

[64] Modine F A, Haywood T W and Allison C Y 1985 Optical and electrical properties of single-crystalline zirconium carbide *Phys. Rev. B* **32** 7743–7

[65] Delin A, Eriksson O, Ahuja R, Johansson B and Brooks M 1996 Optical properties of the group-IVB refractory metal compounds *Phys. Rev. B* **54** 1673–81

[66] Kora H H, Taha M, Farghali A A and El-Dek S I 2020 First-principles study of the geometric and electronic structures and optical properties of vacancy magnesium ferrite metall *Mater Trans. A Phys. Metall Mater Sci.* **51** 5432–43